

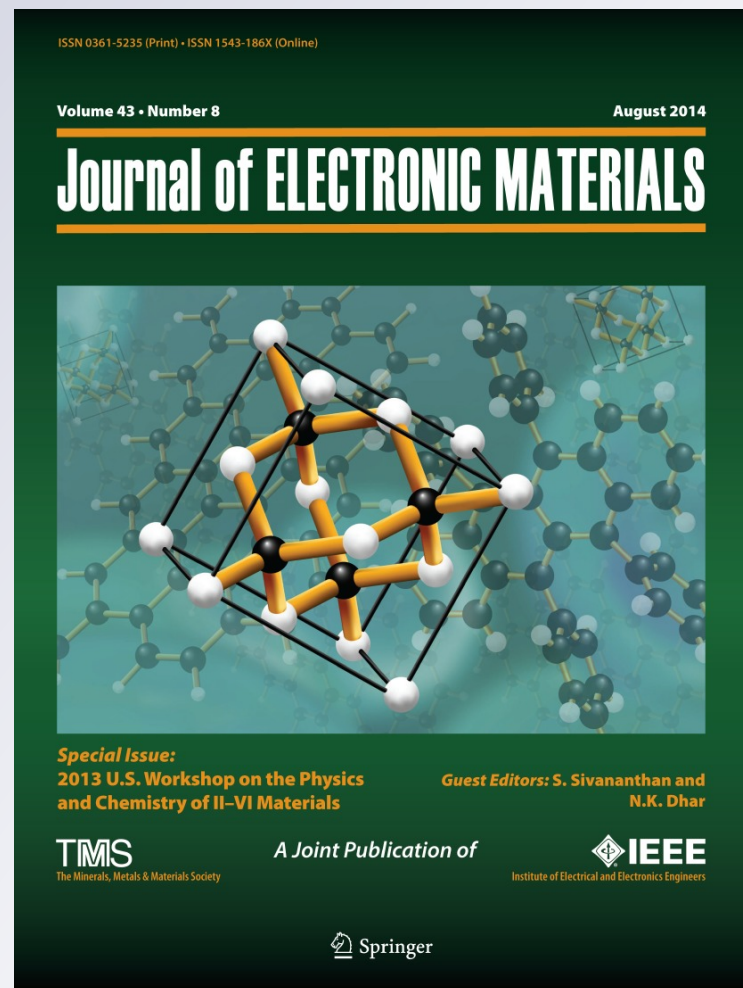
A Highly Sensitive Multi-element HgCdTe e-APD Detector for IPDA Lidar Applications

**Jeff Beck, Terry Welch, Pradip Mitra,
Kirk Reiff, Xiaoli Sun & James Abshire**

Journal of Electronic Materials

ISSN 0361-5235
Volume 43
Number 8

Journal of Elec Materi (2014)
43:2970-2977
DOI 10.1007/s11664-014-3164-8



Springer

Your article is protected by copyright and all rights are held exclusively by TMS. This e-offprint is for personal use only and shall not be self-archived in electronic repositories. If you wish to self-archive your article, please use the accepted manuscript version for posting on your own website. You may further deposit the accepted manuscript version in any repository, provided it is only made publicly available 12 months after official publication or later and provided acknowledgement is given to the original source of publication and a link is inserted to the published article on Springer's website. The link must be accompanied by the following text: "The final publication is available at link.springer.com".

A Highly Sensitive Multi-element HgCdTe e-APD Detector for IPDA Lidar Applications

JEFF BECK,^{1,4} TERRY WELCH,¹ PRADIP MITRA,¹ KIRK REIFF,²
 XIAOLI SUN,³ and JAMES ABSHIRE³

1.—C4ISR Group, DRS Technologies, Inc., Dallas, TX, USA. 2.—Analog/Digital Integrated Circuits, Longwood, FL, USA. 3.—NASA Goddard Space Flight Center, Greenbelt, MD, USA.
 4.—e-mail: jeff.beck@drs.com

An HgCdTe electron avalanche photodiode (e-APD) detector has been developed for lidar receivers, one application of which is integrated path differential absorption lidar measurements of such atmospheric trace gases as CO₂ and CH₄. The HgCdTe APD has a wide, visible to mid-wave-infrared, spectral response, high dynamic range, substantially improved sensitivity, and an expected improvement in operational lifetime. A demonstration sensor-chip assembly consisting of a 4.3 μm cutoff HgCdTe 4 × 4 APD detector array with 80 μm pitch pixels and a custom complementary metal–oxide–semiconductor readout integrated circuit was developed. For one typical array the APD gain was 654 at 12 V with corresponding gain normalized dark currents ranging from 1.2 fA to 3.2 fA. The 4 × 4 detector system was characterized at 77 K with a 1.55 μm wavelength, 1 μs wide, laser pulse. The measured unit gain detector photon conversion efficiency was 91.1%. At 11 V bias the mean measured APD gain at 77 K was 307.8 with σ/mean uniformity of 1.23%. The average, noise-bandwidth normalized, system noise-equivalent power (NEP) was 1.04 fW/Hz^{1/2} with a σ/mean of 3.8%. The measured, electronics-limited, bandwidth of 6.8 MHz was more than adequate for 1 μs pulse detection. The system had an NEP (3 MHz) of 0.4 fW/Hz^{1/2} at 12 V APD bias and a linear dynamic range close to 1000. A gain-independent quantum-limited SNR of 80% of full theoretical was indicative of a gain-independent excess noise factor very close to 1.0 and the expected APD mode quantum efficiency.

Key words: HgCdTe, APD, NEP, IPDA, CO₂, lidar

INTRODUCTION

NASA Goddard Space Flight Center (GSFC) is currently developing an integrated path differential absorption (IPDA) lidar that measure the column absorption of CO₂ at 1572 nm, and CH₄ at 1651 nm as candidates for NASA's active sensing of CO₂ emission over days, nights, and seasons (ASCENDS) space mission. Both the CO₂ and CH₄ lidar measurements have been demonstrated from aircraft. A major technical challenge for the ASCENDS mission has been the lidar detector, which ideally has high photon sensitivity in this spectral region, a large

linear dynamic range, and a long in-space operational lifetime.

GSFC has adapted the DRS HgCdTe electron avalanche photodiode (e-APD) detector for this application. The HgCdTe e-APD is a unique APD that provides high gain and high sensitivity from the visible to infrared (IR) regions. This APD detector is attractive, because its gain is nearly “noiseless” (the excess noise factor is close to unity) and is very uniform.¹ It can provide analog response with sensitivities in the photon counting level from the visible to the mid-IR. This results in improved sensitivity for lidar receivers and for other electro-optical systems applications.

The HgCdTe APD, detector design is based on the highly successful high-density vertically integrated photodiode (HDVIP[®]) architecture. The HDVIP

(Received October 26, 2013; accepted April 2, 2014;
 published online May 10, 2014)

device is a front-side illuminated, cylindrical, *p*-around-*n* photodiode that is formed around a small via in the HgCdTe, shown in Figs. 1 and 2, in which the via serves as the interconnect conduit between the *n*-side of the photodiode and the input to the readout circuit.² The HDVIP structure is currently used in mid-wave infrared and long-wave infrared (LWIR) staring arrays in production at DRS. The reasons for the success of this architecture are:

1. interdiffused CdTe passivation of both surfaces for low $1/f$ noise;
2. thermal cycle reliability that is detector and array size-independent;
3. low defects as a result of diode junction orientation with regard to threading dislocations; and
4. front side illumination for high quantum efficiency from $4 \mu\text{m}$ into the visible region, and good modulation transfer function.²

For APD operation the reverse bias is increased until an electric field sufficient for avalanche multiplication is achieved. At a few volts bias, the *n*-region becomes fully depleted.² Photo-electrons generated in the *p* region diffuse to the *n* region, which is the multiplication region. A unique feature of the HgCdTe e-APD is that holes generated in the multiplication region, for all practical purposes, do not multiply, which results in an ideal $k = 0$ APD, where k is the hole to electron ionization coefficient ratio. Another unique feature of the HgCdTe e-APD is that the multiplication process is largely deterministic^{3,4} which results in an excess noise factor near 1.0.

The HgCdTe e-APD has resulted in high, uniform, exponential gain without breakdown. Also, the HgCdTe e-APD has a gain-independent excess noise factor.¹ These characteristics, exponential gain without breakdown and a gain independent excess noise factor are predicted for an “ideal” $k = 0$ APD. The near 1.0 excess noise factor is the result of a deterministic (history dependent) ionization process.

This performance has been realized in large and small area array formats. Range-gated imaging, 128×128 $40 \mu\text{m}$ pitch, focal plane arrays (FPAs)

had sub-0.5 photon noise-equivalent input sensitivities with median APD gains as high as 946.⁵ Linear mode single-photon detection with high single-photon signal-to-noise ratio (SNR), average value 13.7, less than 1 ns jitter, and a photon detection efficiency near 50% has been demonstrated for a 2×8 array operating at an APD gain near 500.⁶

Initial results on the 4×4 APD sensor chip assembly (SCA), the subject of this paper, were presented at the 2013 SPIE Defense Security and Sensing meeting in April–May 2013.⁷ In this paper we summarize those findings, and provide additional results obtained since then.

DESIGN OF LIDAR DETECTOR Requirements

This application is for an IPDA lidar that transmits $1 \mu\text{s}$ wide laser pulses with ~ 50 ns rise times. Therefore, the design objective was to achieve an optimized noise equivalent power (NEP) for a bandwidth of 3–8 MHz. Based on simulations of read-out integrated circuit (ROIC) performance (discussed in the section “Preamplifier (ROIC)”), an assumed worst-case detector net photon conversion efficiency of 50%, and Dewar optics transmission, we calculated the expected system NEP as a function of APD gain shown in Fig. 3 for the baseline ROIC gain setting and three gain-normalized dark currents (GNDCs). This modeling showed that with this conservative set of assumptions an NEP of $< 5 \text{ fW/Hz}^{1/2}$ could be achieved with APD gains of approximately 100 with an effective GNDC of less than 64 pA, a 9.8 MHz bandwidth, and transimpedance preamp with a gain of 330 kV/A and broadband RMS noise of $340 \mu\text{V}$. NEP performance approaching $1 \text{ fW/Hz}^{1/2}$ was expected for higher APD gains and lower dark currents.

Array and Fanout

The array consisted of a 4×4 arrangement of square $80 \times 80 \mu\text{m}$ pixels on an $80 \mu\text{m}$ pitch. The array was fabricated on a SiO_2/Si fanout that provided connections from the array to bond pads

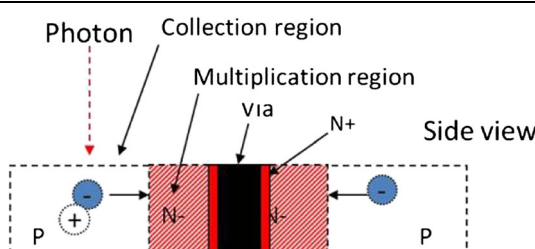


Fig. 1. HDVIP APD cross section. The *p* region is the absorption region and the *n*-region is the multiplication region.

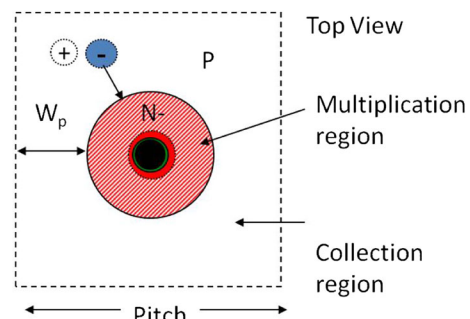


Fig. 2. Top view of HDVIP APD unit cell.

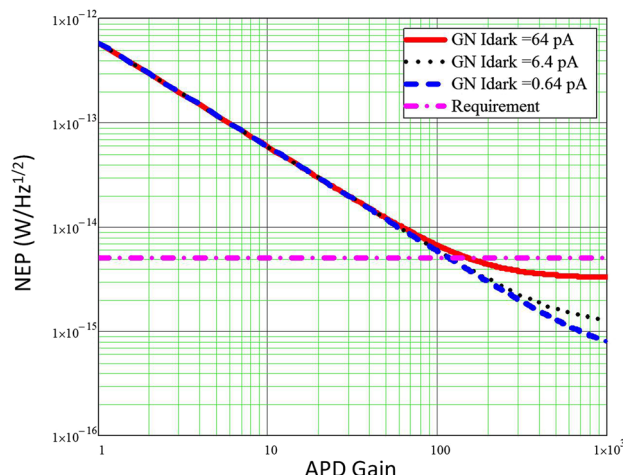


Fig. 3. Predicted NEP for 9.8 MHz bandwidth.

for interconnection to the ROIC. The array is surrounded by a ring of guard diodes surrounded by a substrate contact ring. Each pixel consists of four APDs on a $40\text{ }\mu\text{m}$ pitch, in a 2×2 arrangement, connected in parallel by means of underlying metallization on the fanout. The target diameter for the junction was $22\text{ }\mu\text{m}$. The fanout was designed to provide a minimum stray input capacitance from the detector, to the bond pads. To do this, minimum trace lengths and trace widths, and small bond pads, were used.

Preamplifier (ROIC)

The ROIC is a custom complementary metal oxide semiconductor (CMOS) design that uses $0.18\text{ }\mu\text{m}$ design rules. The unit cell consists of a resistive transimpedance amplifier (RTIA) connected to the cathode of the APD that provides signal input. Three selectable feedback resistors set the option of seven transimpedance gain values. There is also the option of running in a capacitive transimpedance amplifier (CTIA) mode. The preamp is followed by a sample and hold circuit and a post-amp buffer stage with three selectable gain settings of 1 V/V , 2 V/V , and 4 V/V . The sample and hold is used in the CTIA mode. The combination of the preamp and post amp gain selections results in 21 possible full-path transimpedance gains in the design that range from $47.7\text{ k}\Omega$ to $1325\text{ k}\Omega$, a factor of 27.8. The design baseline was a full path gain of $331\text{ k}\Omega$ with a $1\times$ buffer gain setting. End-to-end performance simulations were conducted which assumed a worst-case input capacitance. These simulations predicted that the bandwidth would range from 21.9 MHz at the lowest gain to 8.9 MHz at the highest gain. The baseline design gain was $331\text{ k}\Omega$ at 80 K ; the predicted full path integrated noise was $336\text{ }\mu\text{V}$; the 3 dB signal bandwidth was 9.77 MHz ; and the shot noise was $115.2\text{ fA/Hz}^{1/2}$ at 100 kHz .

The noise bandwidth was predicted to be 1.17 times the signal bandwidth.

The ROIC passed room temperature design verification testing at 25 C in RTIA mode with measured performance very close to simulation predictions. The pulse rise time, with the $320\text{ k}\Omega 1\times$ post amp gain setting, implies a bandwidth of 9.2 MHz which is close to the predicted cold value of 9.8 MHz . Dynamic range measurements revealed a 2 V peak-to-peak swing. With an adjustable APD gain from 1 to 300 and the minimum to maximum ROIC gain, the dynamic range is expected, from the noise level, to be greater than 70 dB .

At DRS the ROIC was tested with a detector array. Proper operation, gain setting functionality, noise, and bandwidth were verified. With an $8\times$ gain buffer board, the measured broadband noise with the baseline preamp gain settings was $302\text{ }\mu\text{V}$ which is lower than the predicted simulation value of $336\text{ }\mu\text{V}$. The rise time with this gain setting was 51 ns for a bandwidth of 6.8 MHz .

Dewar and Optics

A closed cycle, reconfigurable, Dewar with a 1.5 W cryocooler was selected for operation at temperatures near 80 K . The cold shield was designed to accommodate a F/1.5 optical cone and a 25.4 mm diameter cold filter. A $1.2\text{--}1.8\text{ }\mu\text{m}$ bandpass filter with $>\text{OD } 4.0$ blocking from $3\text{ }\mu\text{m}$ to $5\text{ }\mu\text{m}$ was selected for testing with $1.55\text{ }\mu\text{m}$ laser signals at DRS. The Dewar had two multi-pin connectors for I/O.

Electronics and Software

A custom set of four electronic printed circuit boards were designed and fabricated:

1. an internal Dewar board;
2. an external Dewar interface card with buffers for the analog signals;
3. a second external Dewar interface card for digital control and power; and
4. a power, command, and control, side-board.

The internal Dewar board holds the 68 pin leadless chip carrier (LCC) and provides the electrical interface between the LCC and the two Dewar connectors. The two external Dewar interface cards are attached directly to the two Dewar connectors. The side-board is connected to the interface cards with ribbon cables. Field-programmable gate array firmware and software were written to provide control by use of a laptop computer connected by a universal serial bus port to the side-board. Two analog buffer cards were fabricated: one with a $1\times$ gain into $50\text{ }\Omega$ and another with an $8\times$ gain.

4×4 ARRAY FABRICATION AND TEST

A fabrication lot (A8052) was run at DRS (Dallas) with 96 4×4 arrays on 16 HgCdTe chips. The

Table I. GNDC at 10 V of five “perfect” fanout arrays (gain of 160 assumed)

Array	Median GNDC (fA)	Max GNDC (fA)	Max GNDC (center 4) (fA)
4E	1.64	3.94	1.7
11D	1.43	20.4	8.53
7C	0.883	8.11	1.7
13E	3.49	66.8	66.8
16B	4.48	6180	2.71

measured junction diameter on witness samples was $22.4 \mu\text{m}$. In our analysis below, this diameter is rounded up to $23 \mu\text{m}$. The arrays were screened by measuring dark current voltage data out to 10 V on four pixels of each array at 77 K. Sixty-six arrays (69%) met the dark current requirement in the four pixels. Eleven of these were selected for full 16 pixel characterization. Five “perfect” arrays were found in which all 16 pixels met 6.4 pA maximum GNDC spec at 10 V where the APD gain was assumed to be approximately 160.* The data are summarized in Table I. Four of these five arrays had pixels with GNDCs no higher than 67 fA. The center four pixels in three arrays had GNDCs less than 8.6 fA, that is almost 0.1% of the baseline design requirement.

Gain and dark current were measured as a function of bias on several arrays. Array A8052-2C had a gain of 173 at 10 V. The GNDC at 10 V was approximately 4 fA, which is well below the flow-down baseline requirement of 6400 fA. A8052-2A had a gain at 10 V of 157 and a GNDC of 18 fA. Another fanout array, A8052-15D, was measured for gain and dark current out to 12 V. The data shown in Figs. 4 and 5 reveal a gain of 144 at 10 V, a gain of 654 at 12 V, and a GNDC of 1.2–3.2 fA at 12 V. In conclusion, on the basis of dark current and gain measurements, the 4×4 fanout lot produced excellent dark current results with very good yield. On the basis of the model shown in Fig. 3, noise bandwidth normalized system NEPs of $1 \text{ fW}/\text{Hz}^{0.5}$ were predicted to be within reach.

The five selected fanout arrays were integrated with tested ROIC chips in a 68 pin LCC. The layout on the LCC is shown in Fig. 6. Array A8052-4E was selected for test and delivery with the system.

*The gain of 160 used in the calculation of gain normalized dark current is based on measured gains from 157 to 173 on two arrays 2A and 2C from this lot. It should be fairly close to the gain for all arrays in the lot, because the cutoffs are the nearly the same ($4.27\text{--}4.35 \mu\text{m}$).

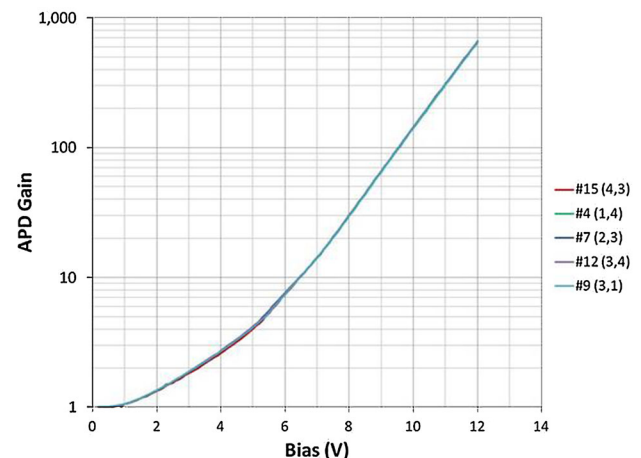


Fig. 4. Gain versus voltage on four pixels from detector array A8052-15D to 12 V. Gain of 654 at 12 V.

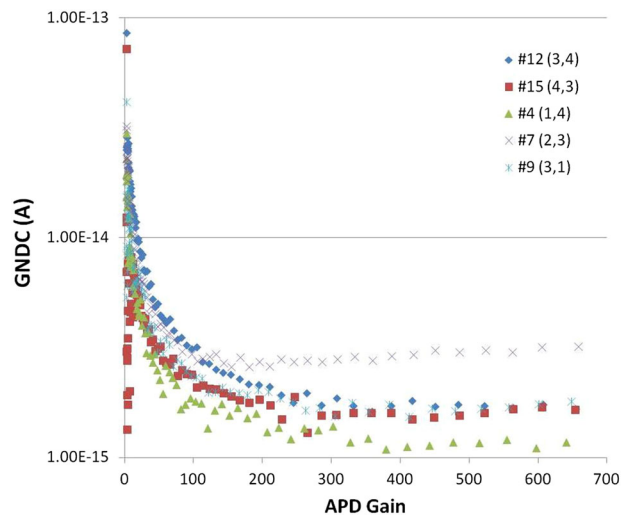


Fig. 5. GNDC density versus gain on pixels from detector array A8052-15D. (Below a gain of approximately 200 the dark currents were below the system measurement limit).

SCA TEST RESULTS

Test Results on Delivered SCA

The 4×4 array detector system, consisting of the Dewar, cooler, optics, electronics boards, and SCA, was assembled. The assembled system and test configuration are shown in Fig. 7. The test signal was provided by a $1.55 \mu\text{m}$ fiber laser with a $1 \mu\text{s}$ pulse width.

Before delivery, we performed some basic characterization measurements at DRS. The system test conditions are summarized in Table II. Shown in Fig. 8 is the measured APD gain versus bias on one of the pixels, pixel 9 (row 3, column 1) at 77 K. The gain at 10 V was 141 and at 11 V it was 297. The photon-to-electron conversion efficiency, CE, at unit gain was calculated from the measured signal data at a bias of 0.5 V where the APD gain is 1. The

calculation assumes the expected end-to-end gain of 330 kV/Amp based on the measured room temperature values with a predicted 3% increase at 77 K. The data show an average pixel CE of 91.1% and a 1.5% σ/mean uniformity. The low gain CE reflects photo-signal contributions from both the *n* and *p* sides of the junction (discussed further in the next section).

Note, the term “photon-to-electron conversion efficiency” used here is what is commonly referred to as “quantum efficiency”. We prefer to break the “quantum efficiency”, or what we define as “conversion efficiency”, into its fundamental components. We define the conversion efficiency as the product of the quantum efficiency, the optical fill factor, and the minority carrier collection efficiency. The quantum efficiency is defined here as the ratio of the number of photo-generated hole–electron pairs to the number of incident photons in the HgCdTe active region. The quantum efficiency, as

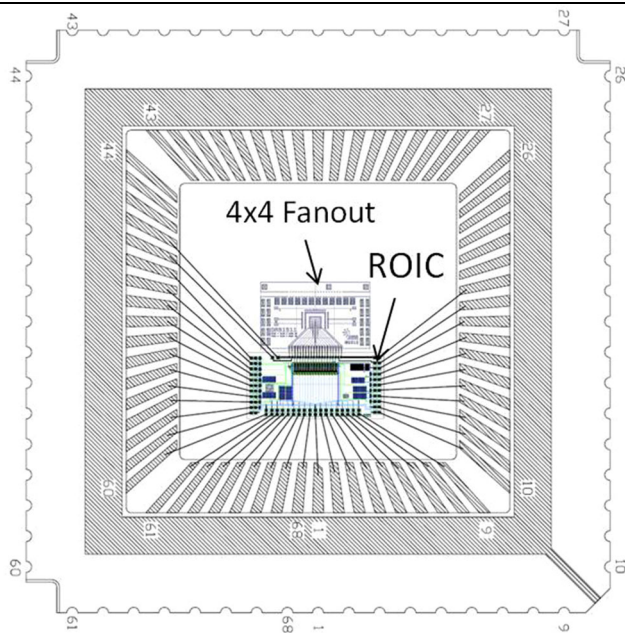


Fig. 6. SCA layout. The 4×4 array is centered in the LCC.

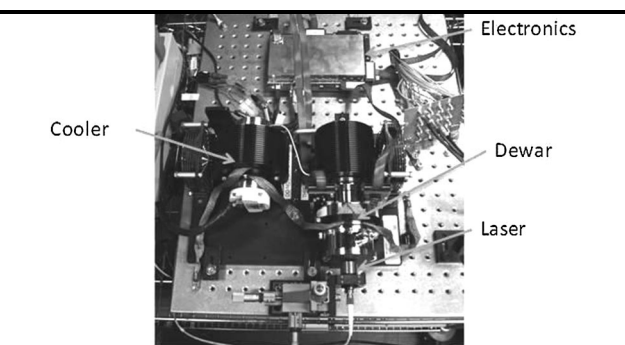


Fig. 7. The 4×4 APD array detector system test configuration at GSFC.

we define it, depends on the AR coating, the thickness of the HgCdTe, the wavelength of the incident radiation, and the absorption coefficient. The minority carrier collection efficiency reflects the effect of minority carrier recombination loss, and the optical fill factor is the fraction of the pixel area which is light-sensitive.

The rise times were measured on all 16 pixels at 77 K with a 10 V bias applied. The rise times varied from 49.6 ns to 51.8 ns with an average of 50.9 ns for a bandwidth of 6.79 MHz. The noise bandwidth used in the NEP/Hz $^{1/2}$ calculations was estimated from ROIC simulations to be 8.14 MHz. Shown in Fig. 9 is the measured gain at 10 V and 11 V on all pixels at 77 K. At 10 V the APD gain was 146.0 with a σ/mean of 1.31%. At 11 V the average gain increased to 307.8 with a σ/mean of 1.23%.

We measured the system NEP at APD biases of 10 V and 11 V at 77 K with an external buffer gain of 8 V/V. The average responsivity at 11 V was 782.0 $\mu\text{V/pW}$ with a 1.8% σ/mean . The corresponding detector responsivity at 11 V was 355 A/W. The average broadband NEP at 11 V was 2.97 pW. The estimated NEP/Hz $^{1/2}$ was calculated by dividing the NEP by the noise bandwidth which is estimated to be 1.2 times the signal bandwidth. The NEP for

Table II. Test conditions for NEP data

Property	Value	Units
Signal wavelength	1.55	μm
Signal pulse width	1	μs
Signal amplitude	<2–100	nW
Operating temperature	77	K
ROIC preamp gain	330	k Ω
ROIC postamp gain	1	V/V
Dewar buffer card gain into 1 M Ω	8	V/V
Cold filter pass band	1.2–1.8	μm
Cold filter transmission @ 1.55 μm	86	%
Cold filter blocking 3–5 μm	OD4	NA
Dewar window transmission	97	%

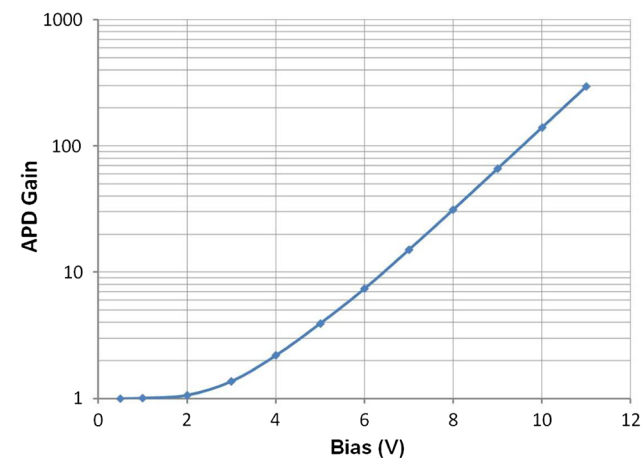


Fig. 8. Gain versus Bias for A8052-4E pixel 9 at 77 K.

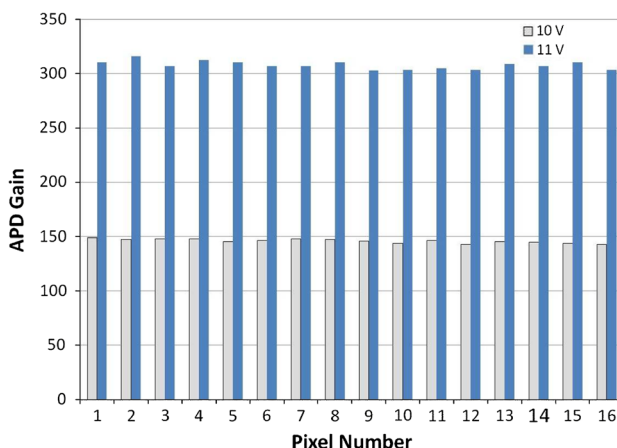


Fig. 9. APD gain at 10 V and 11 V versus pixel at 77 K for array A8052-4E.

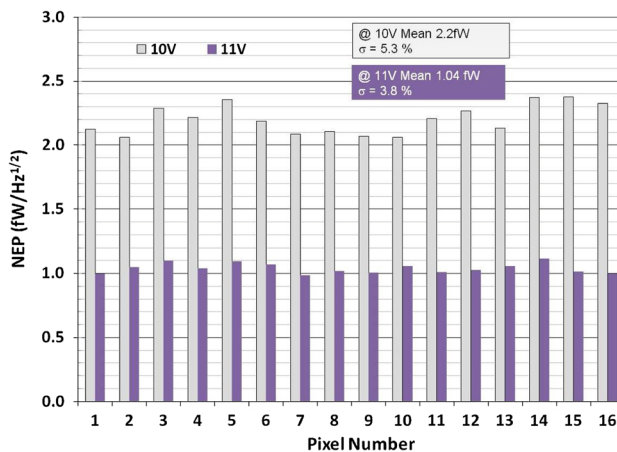


Fig. 10. System NEP versus pixel at 10 V and 11 V at 77 K (A8052-4E).

each pixel, shown in Fig. 10, indicates an average NEP at 11 V of 1.04 fW/Hz^{1/2} with a 3.8% σ /mean and 100% pixel operability with no pixel having an NEP less than 1.12 fW/Hz^{1/2}.

At 10 V the APD gain decreased to 145 and the NEP increased to 2.20 fW/Hz^{1/2}. This indicates that the NEP is changing directly with APD gain. Therefore, further reduction in the NEP is expected with increased bias beyond 11 V.

Test Results at NASA GSFC

Measurements at GSFC verified and added to the results obtained at DRS. The measured NEP/Hz^{1/2} and responsivity versus APD bias, plotted in Fig. 11, shows an NEP at 3 MHz of 0.7 fW/Hz^{1/2} at 11 V and 0.4 fW/Hz^{1/2} at 12 V.

A near-linear dynamic range over three orders of magnitude was measured, as shown in Fig. 12. In this case the dynamic range was measured at the highest ROIC transfer gain of 331 kV/A (77 K gain) and an post-amp gain of 1 and the APD gain of 308

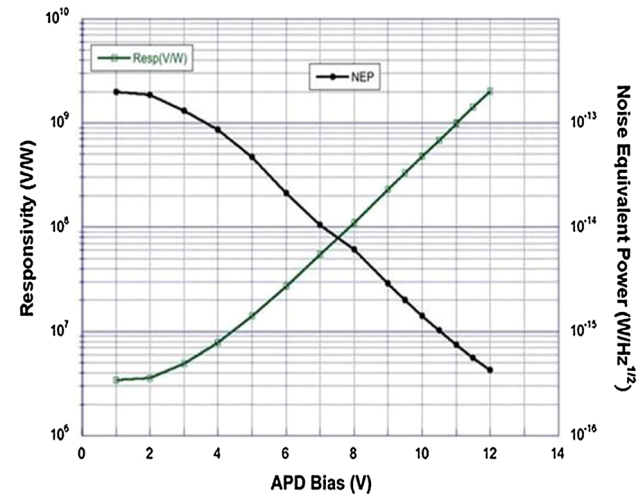


Fig. 11. Measured responsivity and NEP (W/Hz^{1/2}) at 1.55 μ m at 3 MHz versus bias.

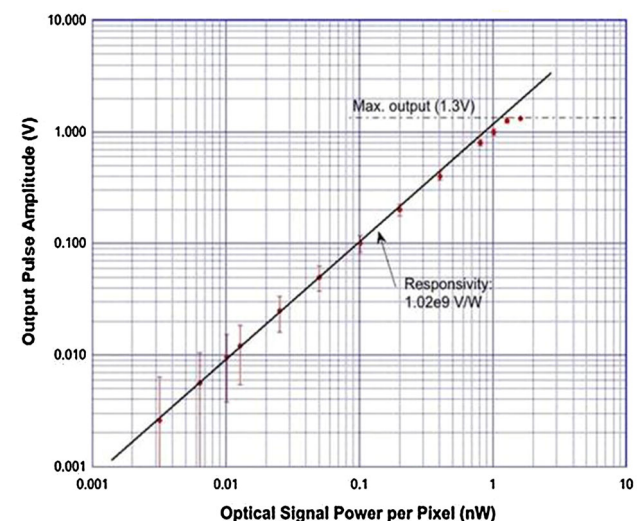


Fig. 12. Dynamic range: output pulse amplitude versus incident power/pixel at 11 V.0 APD bias, 1 μ s rectangular pulse.

corresponding to 11 V bias. The 1.3 V upper limit of the dynamic range was limited by the swing of the external buffer amplifier.

Measurements at GSFC of the detector's SNR versus APD bias for three signal levels are shown in Fig. 13 where both the signal and noise are measured under flux. It was seen that the SNR reached a constant, gain independent, limiting value that was approximately 81% of the quantum limit, QL. The bias independence in the high-bias region of Fig. 13 is because of the gain independence of the excess noise factor.

The quantum limit for an APD is given by:

$$QL = \sqrt{\frac{CE_{APD}}{F(M)}} \quad (1)$$

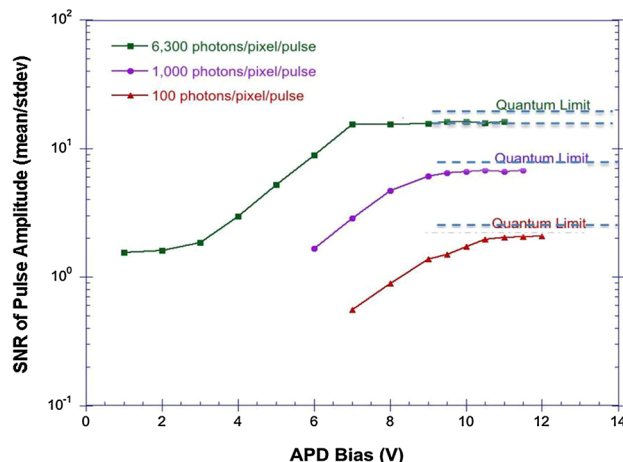


Fig. 13. Measured SNR versus bias showing quantum limit with 1 μ s rectangular pulse.

Table III. Operating conditions for detector NEP characterization

Condition	Value	Comment
FPA temperature	77 K	Initial setting during cooler check-out
ROIC gain	331 k Ω	Predicted for 80 K (320 k Ω @ 300 K)
ROIC post amp gain	1	
Buffer gain	8	50 Ω load
Laser pulse width	1 μ s	

where CE_{APD} is the photon-to-electron conversion efficiency of the APD and $F(M)$ is the true excess noise factor, defined in Ref. 2. The net photon to electron conversion efficiency of the APD at high gains, CE_{APD} is given by:

$$CE_{APD} = FF_{APD} \times QE \times eCE \quad (2)$$

where FF_{APD} is the fill factor of the APD at high gains which excludes the area of the essentially optically inactive multiplication region (n -region) and via (Fig. 2), QE is the quantum efficiency, and eCE is the electron collection efficiency. Assuming a 23 μ m diameter multiplication region (n -region), the APD fill factor is 74%.** With a quantum-limited SNR of 16 (0.813 of full theoretical), an APD fill factor of 0.74, and an eCE of 0.94 (derived from the measured CE of 0.911 at a gain of 1), the estimated CE_{APD} is 0.68 and the estimated excess noise factor is 1.03. The major source of error in this analysis is the assumption of the junction diameter which is based on witness sample measurements.

**The “APD fill factor” is the fill factor predicted from the estimated 23 μ m n -region diameter (rounded up from the measured 22.4 μ m) and the 40 \times 40 μ m APD pitch where the n -region is assumed to be optically inactive and the electron collection efficiency is assumed to be 1.0.

Table IV. System performance at 1.55 μ m with baseline RTIA gain setting

Property	Value	Comment
APD bias	11 V	Applied to all pixels
APD gain	308	Average
NEP @ 1.55 μ m	2.97 pW	Broadband NEP
NEP/ $Hz^{1/2}$	1.04 fW/ $Hz^{1/2}$	Normalized to noise bandwidth
Responsivity @ 1.55 μ m	782 μ V/PW	At system output
Noise at 11 V	2.32 mV	At system output (gain of 8)
System noise (@ 0.5 V)	2.41 mV	At system output (gain of 8)
Bandwidth	6.8 MHz	51 ns rise time
Noise bandwidth	8.1 MHz	Based on predicted 1.2 factor

It should be noted that the photon-to-electron conversion efficiency of the APD at high gains, CE_{APD} , is lower than the CE of 91% measured at low bias (discussed in the section “Test Results on Other SCAs”), where the APD gain is unity. The CE at low bias is higher because at low bias both n and p regions of the pixel contribute to the signal and the fill factor is the approximately the APD unit cell minus the area of the via.[†] At high gains the n -region is essentially optically inactive^{2,6} which effectively reduces the APD filter factor compared with its unit gain value. This is why, for the pixel geometry shown in Fig. 2 and flood illuminated conditions, the CE_{APD} at high gains is lower than the CE at unit gain.²

Test Results on Other SCAs

The four remaining SCAs were measured at DRS in a second system. The system is identical with the first except the buffer gain was 10.7 instead of 8. All four SCAs exceeded the 5 fW/ $Hz^{1/2}$ requirement by a large margin with 100% pixel NEP operability (no pixels in any array having a max NEP greater than 20% of the mean NEP for that array). The range of demonstrated NEPs varied from 1.60 fW/ $Hz^{1/2}$ to 0.62 fW/ $Hz^{1/2}$. Two of these SCA were tested at 12 V APD bias and both achieved measured mean broadband noise-normalized NEPs less than 1 fW/ $Hz^{1/2}$.

One of these SCAs had a mean broadband noise-bandwidth normalized NEP of 0.66 fW at 12 V which seemed to be limited by a very low back-

[†]This approximation assumes the electron and hole diffusion lengths are large compared with the p and n region dimensions. The high CE measured at unit gain suggests this is a valid assumption.

ground flux in the Dewar. Even though the SCAs were designed for 1 μs wide, multi-photon, pulse detection, good single photon sensitivity with SNRs of greater than 3 was predicted for high APD gains. Indeed, single-photon sensitivity was seen in this array at 12 V, where the APD gain was 800, with an average single-photon SNR of approximately 4. The photon events showed up as positive going pulses that stood out significantly over the otherwise Gaussian noise. Because of the purposely limited bandwidth in the ROIC, the width of the pulses was approximately 60 ns. We would see, on average, approximately three such events in a 2- μs period. The count rate of these pulses was increased substantially by turning on the lights in the test laboratory. Similar behavior was seen for the other SCAs. A paper that discusses this single-photon sensitivity will be published.⁸

SUMMARY

We have developed and characterized a new, highly sensitive, 4×4 HgCdTe e-APD array optimized for 1 μs lidar pulse detection and packaged with Dewar, cooler, and electronics. The APD fabrication process resulted in high array yield, very low dark currents, and 100% pixel NEP operability on the five assembled SCAs whereby all the pixel NEPs were tightly distributed about the mean NEP.

For the set of conditions listed in Table III, the measured performance at 77 K of the delivered SCA is summarized Table IV. The delivered SCA has an average NEP of 1.04 fW/Hz $^{1/2}$ at 11 V bias, very good gain, responsivity, and NEP uniformity (100% of the pixels with $\text{NEP} \leq 1.12 \text{ fW/Hz}^{1/2}$). The measured bandwidth was 6.8 MHz (design objective 4 MHz) and the NEP was a factor of five better than the design requirement. The dynamic range for the minimum to maximum ROIC gain and a variable APD gain from 1 to 300 is 70 dB, measured from the

noise level. The measurement results showed good agreement with performance predictions.

FUTURE PLANS

GSFC plans to integrate the delivered detector, Dewar, cooler, and electronics assembly into their airborne IPDA lidar and to demonstrate measurements of CO₂ over horizontal paths and from an aircraft. GSFC also plans to examine and characterize the single-photon sensitivity.

ACKNOWLEDGEMENTS

The authors would like to acknowledge the important contributions of DRS employees James McCurdy (testing), Chris Kamilar (electronics), Mark Skokan (fanout array design), Richard Scritchfield (consulting), Drew Gordon (software), Patty Benken (array fabrication), and Towfik Teherani (management support). This work was supported by the NASA ESTO IIP-10 program managed by Parminder Ghuman and Irene Bibyk.

REFERENCES

1. J. Beck, C. Wan, M. Kinch, J. Robinson, P. Mitra, R. Scritchfield, F. Ma, and J. Campbell, *J. Electron. Mater.* 35, 1166 (2006).
2. J. Beck, et al., *J. Electron. Mater.* 38, 1579–1592 (2009).
3. M. Kinch, *J. Electron. Mater.* 37, 1453 (2008).
4. J. Rothman, L. Molland, S. Goût, and J. Wlassow, *J. Electron. Mater.* 40, 1757–1768 (2011).
5. J. Beck, M. Woodall, R. Scritchfield, M. Ohlson, L. Wood, P. Mitra, and J. Robinson, *Proc. SPIE* 654217, 1–17 (2007).
6. J.D. Beck, R. Scritchfield, P. Mitra, W. Sullivan III, A.D. Gleckler, R. Strittmatter, and R.J. Martin, *Proc. SPIE* 80330N, 1–15 (2011).
7. J. Beck, J. McCurdy, M. Skokan, C. Kamilar, R. Scritchfield, T. Welch, P. Mitra, X. Sun, J. Abshire, and K. Reiff, *Proc. SPIE* 8739, 87390V (2013).
8. X. Sun, J. Abshire, and J.D. Beck, *SPIE Conference Proceedings, Conference 9114, Advanced Photon Counting Techniques VIII, paper 19* (2014) (to be published).